Electronic Supplementary Informaterial

Regulating from Local Electron Density to Adsorption Energy of COF-based Single Copper Sites for Highly Efficient Fenton-like Photo-oxidation

Qianqian Peng[a], Guijiao Wen[a], Chen Yuan[a], Caizhi Lv[a], Lan Wu[a], Juan He[a]*, Xiandeng Hou[a, b]*

[a]Analytical & Testing Center, Sichuan University, Chengdu 610064, Sichuan, China

[b]College of Chemistry, and Key Lab of Green Chem and Tech of MOE at Sichuan University, Chengdu 610064, Sichuan, China

*Corresponding authors' E-mails: houxd@scu.edu.cn; hejuan1117@scu.edu.cn

Experimental Procedures

Materials

All reagents were of at least analytical grade. Deionized water (DIW, 18.2 MΩ cm) obtained from a water purification system (Sichuan Pincheng Technology Co. Ltd., Chengdu, China) was used to prepare all solutions here. Copper acetate (Cu(OAc)$_2$) and dimethyl pyridine N-oxide (DMPO) were purchased from Chron Chemicals (Chengdu, China). Carbamazepine (CBZ), methanol (MeOH), formic acid (FA), *p*-benzoquinone (*p*-BQ), *tert*-butyl-alcohol (TBA), acetic acid (AcOH) and peroxymonosulfate (PMS) were obtained from Aladdin Reagent Co. Ltd (Shanghai, China). 1,3,5-Triformylphloroglucinol (Tp), *p*-phenylenediamine (Pa), 2,5-diamino-*p*-xylene (Pa-(CH$_3$)$_2$) and 2-(aminomethyl)benzonitrile (Pa-CN) were from McLean BioReagents (Shanghai, China). Rhodamine 6G (R6G), Phenylbenzimidazole (PBSA) and ciprofloxacin (CIP) were obtained from Aladdin Reagent Co. Ltd (Shanghai, China).

Preparation of Catalyst

1,3,5-Triformylphloroglucinol (Tp, 63 mg, 0.3 mmol) and 2, 5-diamino-p-xylene (Pa-(CH$_3$)$_2$, 60.5 mg, 0.45 mmol) were dispersed in 2 mL of N, N-dimethylformamide (DMF) and 0.2 mL acetic acid (AcOH). The mixture was then sonicated for 15 min and transferred into the reactor of dielectric barrier discharge (DBD) plasma.[1] The plasma reactor was then evacuated and replenished with N$_2$, and discharged for 40 min at a voltage a 30 V and a current of 1.20 A. The obtained product was filtrated and washed with anhydrous tetrahydrofuran. The filtered solid powder was vacuum dried at 80°C for 12 h to produce TpPa-(CH$_3$)$_2$ with approx 91% isolated yield. The Tp-based COFs (TpPa, TpPa-CN) were prepared in the same procedures but with Pa and Pa-CN replacing the Pa-(CH$_3$)$_2$ monomer, as shown in Figure 1.

In a typical synthesis procedure for Cu@TpPa-(CH$_3$)$_2$, TpPa-(CH$_3$)$_2$ (20 mg) was dispersed in 20 mL mixed solvent (CH$_3$OH: H$_2$O =1:1 v/v), and Cu(OAc)$_2$·5H$_2$O (10 mg) was added into TpPa-(CH$_3$)$_2$ suspension at a rate of 2 mL/min under magnetic stirring at room temperature. The suspension was stirred at 300 rpm for 8 h. The resultant product

was washed with methanol and water, and vacuum dried at 80°C for 12 h. Cu@TpPa and Cu@TpPa-CN were prepared in the same method but with TpPa and TpPa-CN replacing the TpPa-$(CH_3)_2$, respectively.

Analysis and characterization

The Cu content of Cu@TpPa-X (X=H, CN, $(CH_3)_2$) was determined with an inductively coupled plasma-optical emission spectrometer (ICP-OES, 5100 SVDV Series, Agilent, USA). The powder X-ray diffraction (PXRD) patterns were collected in the 2θ range between 2°and 40° with an X'Pert Pro MPD (Panalytical, Netherlands). The UV-Vis absorption spectra and X-ray photoelectron spectra (XPS) were obtained from a UV-Vis spectrophotometer (UV-1750, Shimadzu, Japan) and an X-ray photoelectron spectrometer (AXIS Supra, Kratos, England), respectively. A UV-Vis diffuse spectrophotometer (UV-vis DRS, UV 3600, Shimadzu, Japan) was used to study the optical properties. The Fourier transform infrared (FT-IR) spectra and the photoluminescence (PL) spectra were collected on a Nicolet IS10 Fourier transform infrared spectrometer (Nicolet 6700, Thermoelectronic, America) and a photoluminescence spectrometer (F-7000, HiTachi, Japan), respectively. The scanning electron microscopy (SEM) photos were taken with a scanning electron microscope (JSM-7500F, JEOL, Japan) equipped with an energy dispersive spectrometer (EDS). The transmission electron microscope (TEM) photos and the high angle annular dark field scanning transmission electron microscope (HAADF-STEM) photos were obtained with transmission electron microscope (FEI Tecnai G2 F20 S-TWIN, Hillsboro, America) and double pitch correction transmission electron microscope (Spectra 300, Thermofisher, America). The nitrogen (N_2) gas adsorption-desorption isotherms were measured by using the Brunauer-Emmett-Teller (BET) method on surface area and porosity analyzer (ASAP 2460, Micromeritics Instrument Corp, USA). The electrochemical impedance spectrum (EIS), photocurrent response capacity and Mott-Schottky (M-S) curve were obtained with an electrochemical workstation (AUTO LAB PGSTAT302N, Netherlands) with three electrodes. Total organic carbon (TOC) was measured by a total organic carbon and total nitrogen (TOC/TN) analyzer (Vario TOC select, German Elementar). The measurement of fluorescence lifetime was performed on a steady/transient state

fluorescence spectrometer (FluoroLog-3, Horiba Scientific, French) at an excitation wavelength of 406 nm. Ultra-high-performance liquid chromatographer (UHPLC, Dionex UltiMate 3000 127 Series) coupled with an Orbitrap mass spectrometer (MS, Thermo Scientific, USA) was applied for the determination of intermediate products generated during the photocatalytic process. The radicals of the photocatalysts were detected with an electron paramagnetic resonance spectrometer (EXM plus, Bruker, German) at room temperature.

Theoretical calculation

The first-principles performed all density functional theory (DFT) calculations within the generalized gradient approximation (GGA) using the Perdew-Burke-Ernzerhof (PBE) formulation. The projected augmented wave (PAW) potentials describe the ionic cores and take valence electrons into account using a plane wave basis set with a kinetic energy cutoff of 520 eV. Partial occupancies of the Kohn−Sham orbitals were allowed using the Gaussian smearing method and a width of 0.05 eV. The electronic energy was considered self-consistent when the energy change was smaller than 10^{-5} eV. A geometry optimization was considered convergent when the energy change was smaller than 0.05 eV Å^{-1}. The Brillouin zone integration is performed using 2×2×1 Monkhorst-Pack k-point sampling for a structure. Finally, the adsorption energies (Eads) were calculated as Eads= Ead/sub -Ead -Esub, where $E_{ad/sub}$, Ead, and E_{sub} are the total energies of the optimized adsorbate/substrate system, the adsorbate in the structure, and the clean substrate, respectively.

XAFS measurements

Cu *K*-edge analysis was performed with Si (111) crystal monochromators at the BL14W1 beamlines at the Shanghai Synchrotron Radiation Facility (SSRF) (Shanghai, China). Before the analysis at the beamline, samples were pressed into thin sheets with 1 cm in diameter and sealed using Kapton tape film. The XAFS spectra were recorded at room temperature using a 4-channel Silicon Drift Detector (SDD) Bruker 5040. Cu *K*-edge extended X-ray absorption fine structure (EXAFS) spectra were recorded in transmission mode. Negligible changes in the line-shape and peak position of Cu *K*-edge XANES

spectra were observed between two scans taken for a specific sample. The XAFS spectra of these standard samples (Cu foil, Cu_2O, and CuO) were recorded in transmission mode. The spectra were processed and analyzed by the software codes Athena and Artemis.

The XAFS data were processed according to the standard procedures using the Athena module implemented in the IFEFFIT software packages. The EXAFS spectra were obtained by subtracting the post-edge background from the overall absorption and then normalizing with respect to the edge-jump step. Subsequently, the $\chi(k)$ data of Fourier transformed to real (R) space using a Hanning window ($dk = 1.0$ Å^{-1}) to separate the EXAFS contributions from different coordination shells. To obtain the quantitative structural parameters around central atoms, least-squares curve parameter fitting was performed using the ARTEMIS module of IFEFFIT software packages.

Photocatalytic degradation experiments

The CBZ degradation experiments were conducted on a parallel photocatalysis reactor with a light source of 300 W Xenon lamp (PLS-SXE300, Perfect Light Co., Ltd., Beijing, China, ca. 260 mW/cm^2). An aliquot of 50 mL aqueous solution of CBZ with predetermined concentration of 10 mg/L was placed below the lamp. In the tests, 10 mg catalyst was added into the solution and kept in the dark under constant stirring for 30 min to reach the adsorption-desorption equilibrium. Then, the photocatalytic degradation was initiated by adding PMS solution and turning on the Xenon lamp. At predetermined time intervals, an aliquot of the suspension was collected and filtered through a 0.22 μm nylon filter membrane for analysis with a UV-Vis spectrophotometer, based on the absorption band at 286 nm for CBZ. The pseudo-first-order kinetic equation (Eq. (1)) can be used to quantitatively study the kinetics of CBZ degradation:

$$kt = -\ln(C/Co) \qquad (1)$$

where k is the pseudo-first-order rate constant, t is the reaction time, C is the concentration of CBZ at time t, and C_0 is the initial CBZ concentration.

Results and Discussion
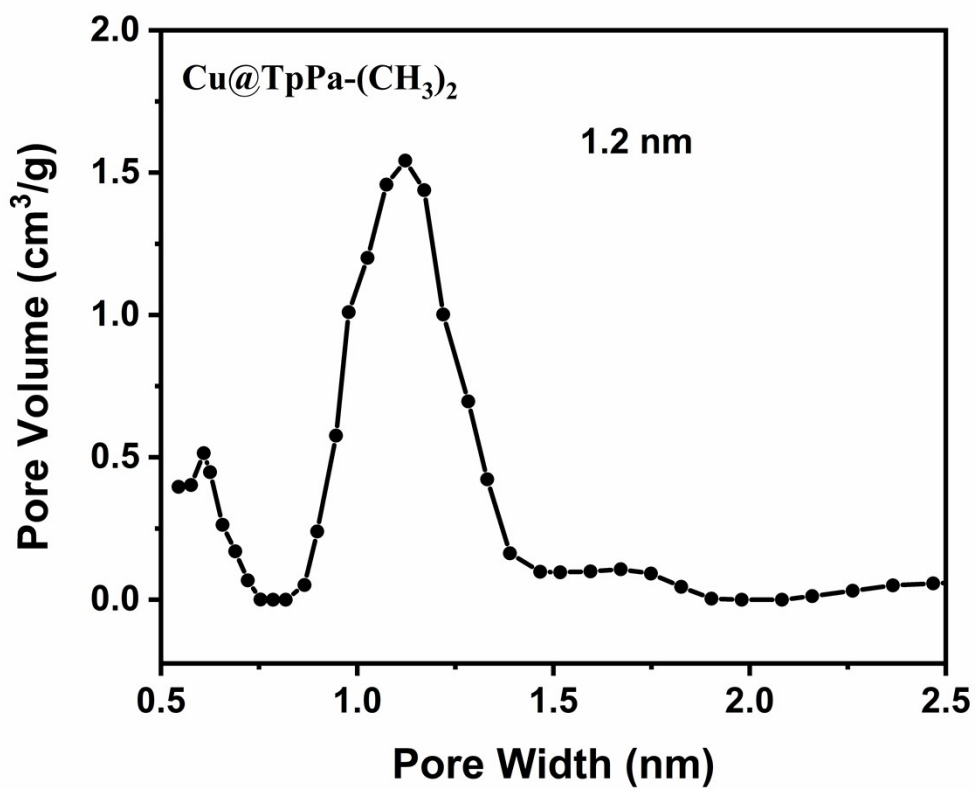
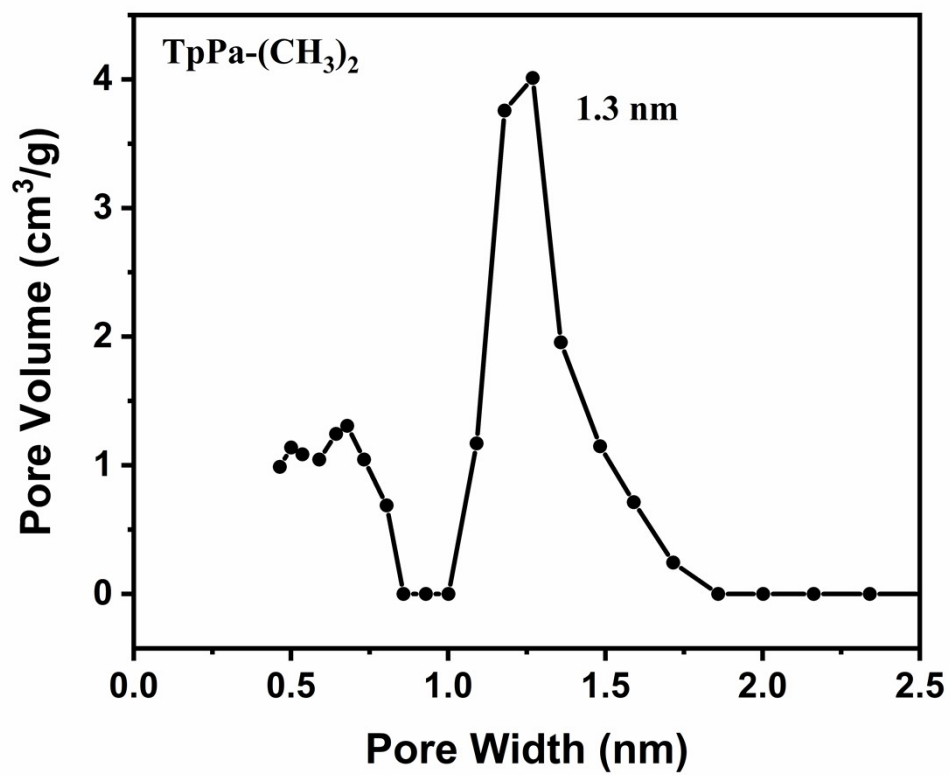**Figure S1.** Pore size distributions of Cu@TpPa-(CH$_3$)$_2$.

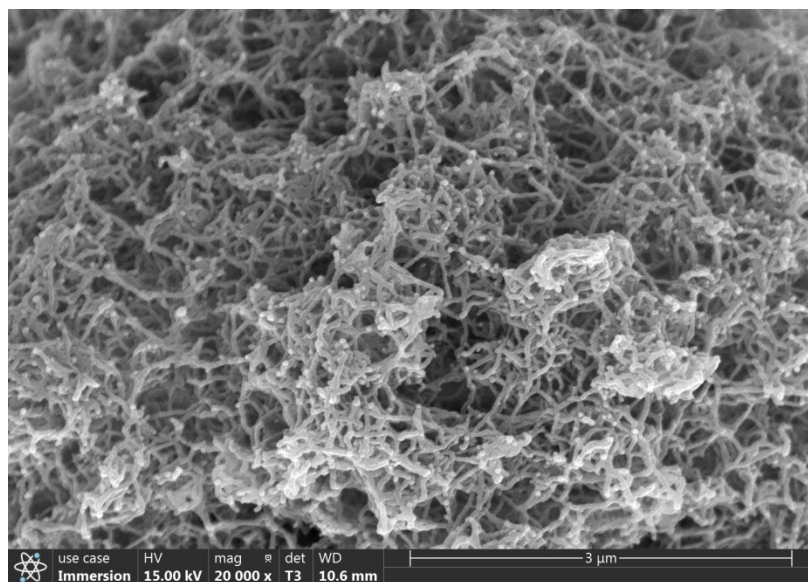**Figure S2**. Pore size distributions of TpPa-$(CH_3)_2$.

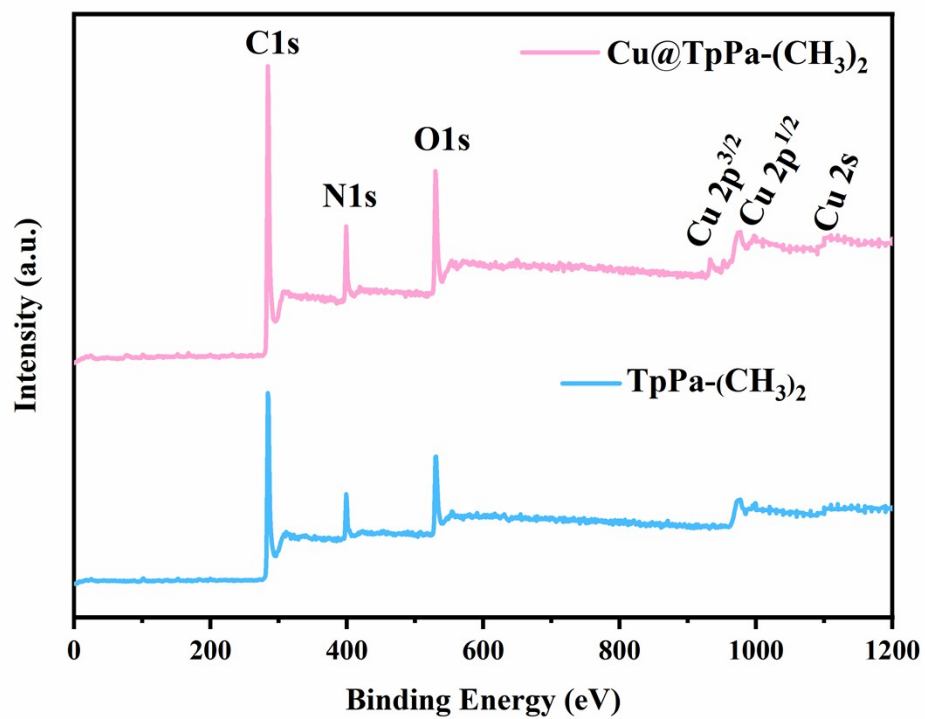**Figure S3**. SEM image of TpPa-$(CH_3)_2$.

Figure S4. XPS full-spectrum image of TpPa-$(CH_3)_2$ and Cu@TpPa-$(CH_3)_2$.
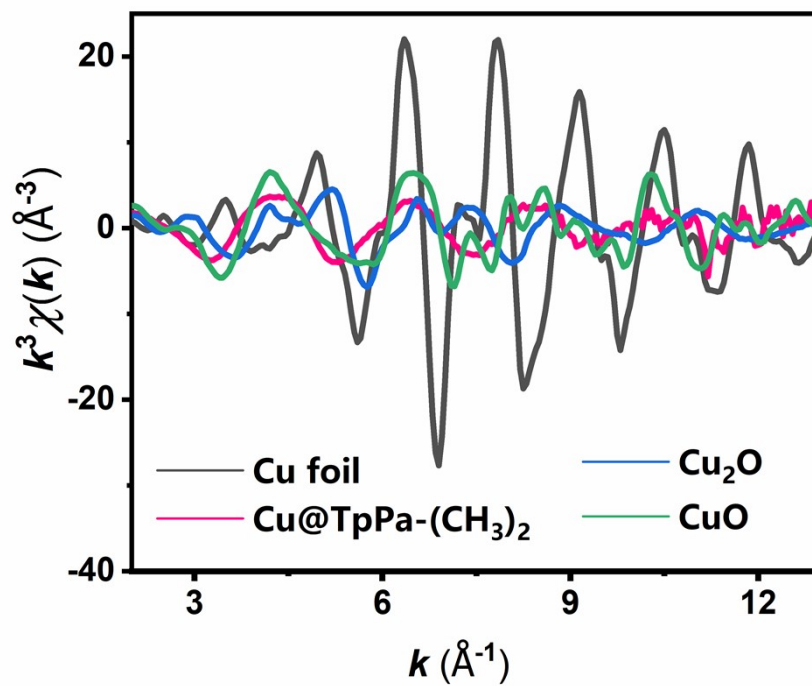
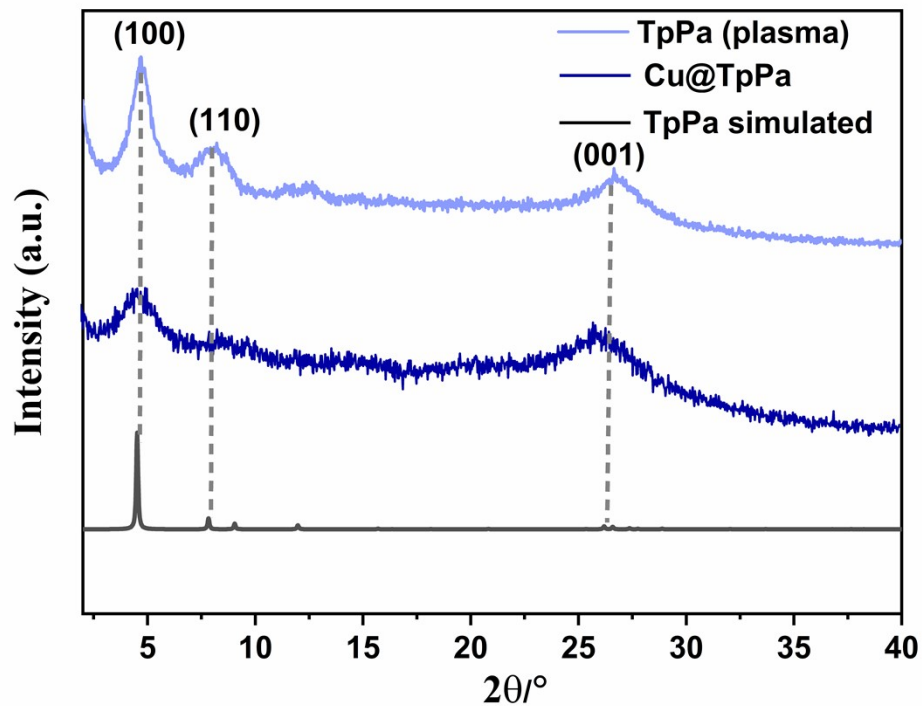**Figure S5**. k^3-weighted spectra at k space of Cu foil, Cu_2O, CuO, and Cu@ TpPa-$(CH_3)_2$.

Figure S6. XRD patterns of TpPa(plasma), Cu@TpPa, and TpPa simulated.

The three intense peaks at 4.6, 8.0, and 26.7° originate from the reflections from the (100), (110), and (001) planes in Cu@TpPa, respectively. All the peaks coincided with the simulated PXPD patterns, suggesting that TpPa should be successfully synthesized in the DBD plasma and the robust COF structure after copper modification, no XRD peaks attributed to crystalline Cu species were detected in samples, which might be due to the uncrystallized single-atom Cu. However, the introduction of Cu atoms may result in lattice distortion, leading to an increase in lattice parameters and lattice spacing, and causing the diffraction peak at 26.7° to shift towards somewhat lower angle at a macroscopic level.
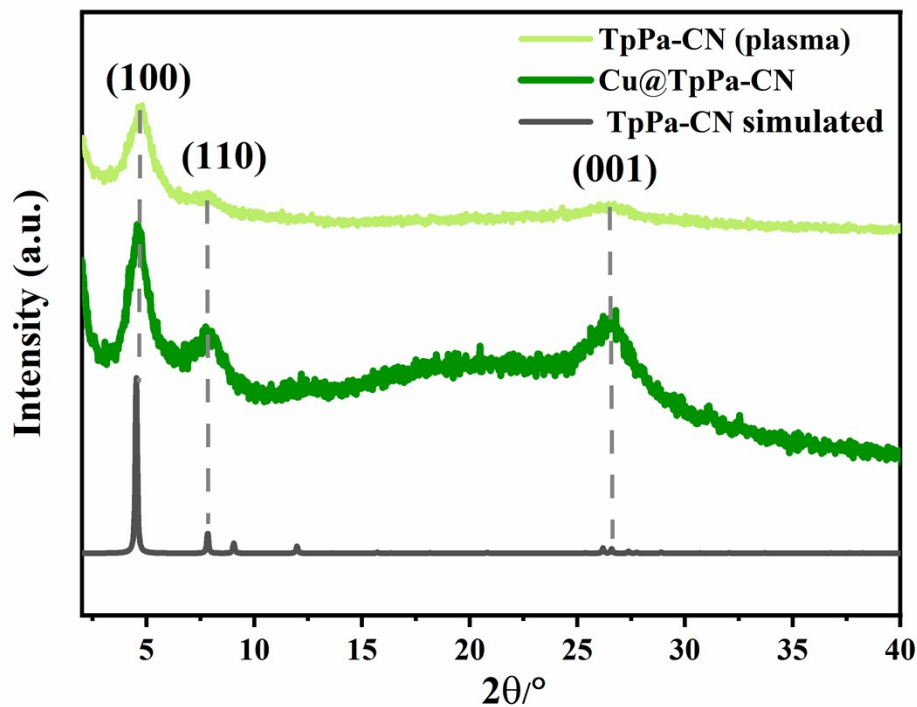
Figure S7. XRD patterns of TpPa-CN(plasma), Cu@TpPa-CN, and TpPa-CN simulated.

The three intense peaks at 4.6, 7.9, and 26.2°attributed to the reflections from the (100), (110), and (001) planes in Cu@TpPa-CN, respectively. All peaks are in agreement with the simulated PXPD pattern, so this can prove the successful synthesis of TpPa-CN in the DBD plasma. There is no significant change in the XRD diffraction peaks after modification of Cu, which proves that the COF skeleton has not collapsed after Cu modification, and there are no diffraction peaks of Cu nanoparticles/clusters, suggesting that no agglomeration of Cu species should have occurred.
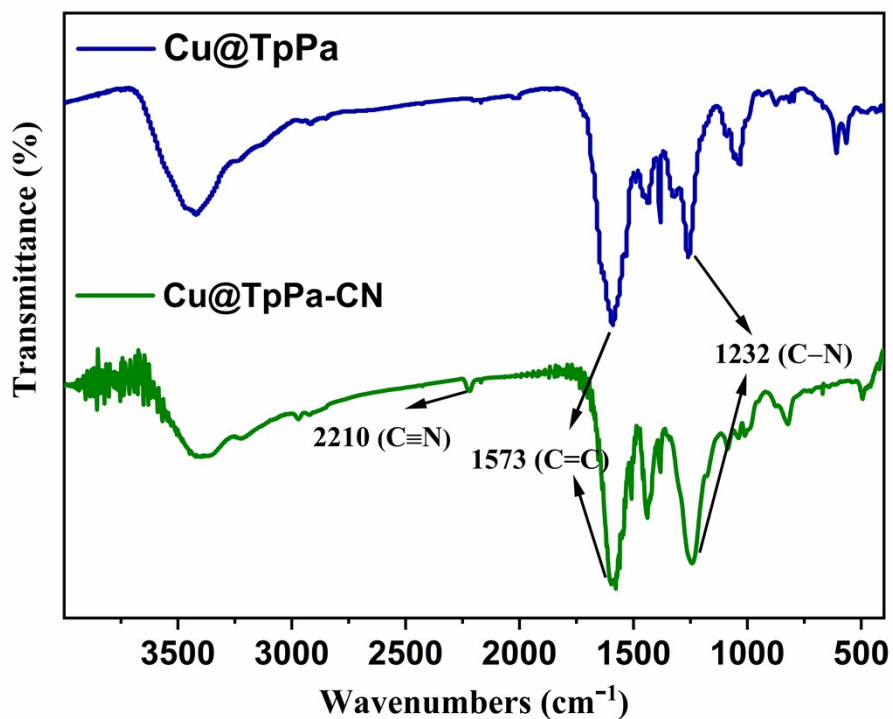
Figure S8. FITR spectrum of Cu@TpPa and Cu@TpPa-CN.

Cu@TpPa and Cu@TpPa-CN show a strong peak at 1573 cm^{-1} originating from C=C stretching, and a peak at 1232 cm^{-1} corresponding to the C-N stretching band, which suggests that they are keto-shaped. In Cu@TpPa-CN, the peak at 2210 cm^{-1} is attributed to C≡N, proving that TpPa and TpPa-CN can be successfully synthesized in the DBD and the robust COF structure after copper modification.
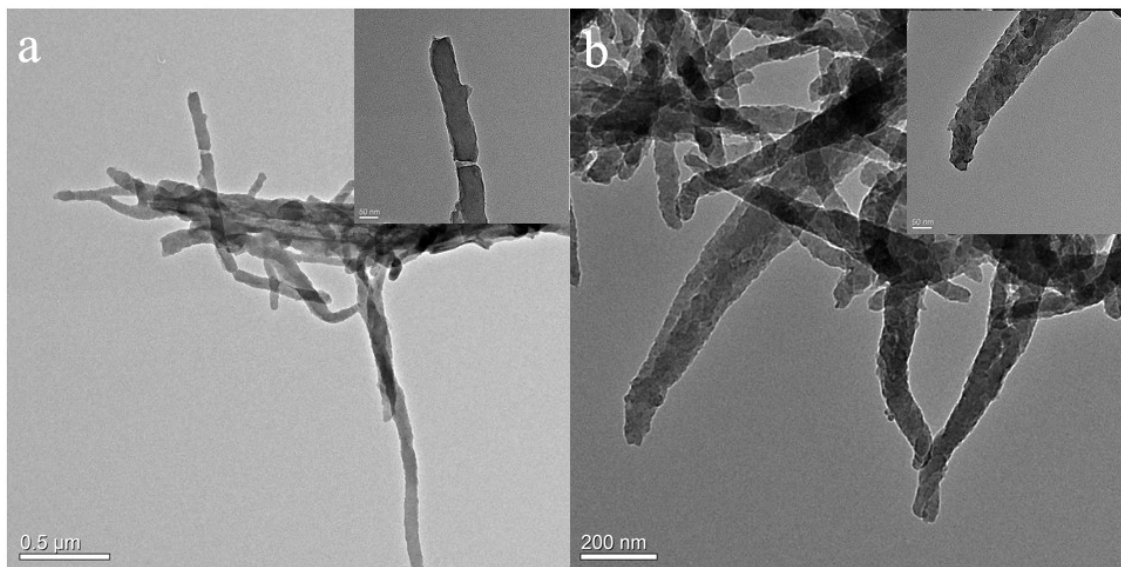
Figure S9. TEM and HRTEM (inset) images of Cu@TpPa (a) and Cu@TpPa-CN (b).

It can be seen that the TEM images of Cu@TpPa and Cu@TpPa-CN show a fibrous morphology, which has a similar morphology to Cu@TpPa-$(CH_3)_2$. No nanoparticles/clusters can be observed from the HRTEM images, which indicates that the Cu species are not reunited.
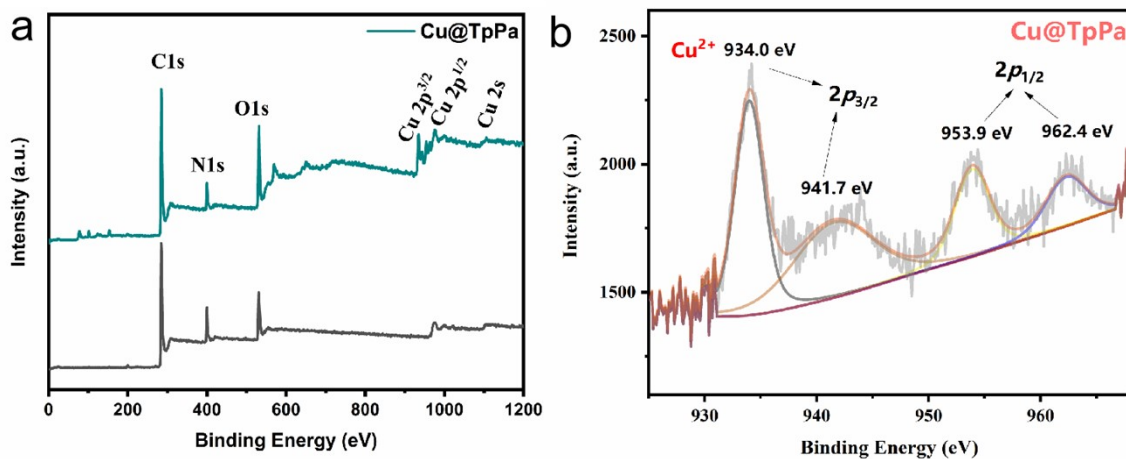
Figure S10. a) XPS full-spectrum image of TpPa and Cu@TpPa. b) High-resolution Cu 2p XPS spectra of Cu@TpPa.

The full spectrum demonstrated the presence of C, N, O, and Cu elements in Cu@TpPa, the binding energy of 934.0 and 941.7 eV attributed to $2p_{3/2}$ of Cu^{2+} signals, and the peaks of 953.9 and 962.6 eV attributed to $2p_{1/2}$ of Cu^{2+} signals, respectively. Combined with the absence of Cu-Cu bonds, it is demonstrated that Cu species should be anchored on the TpPa in the form of single Cu^{2+} site.
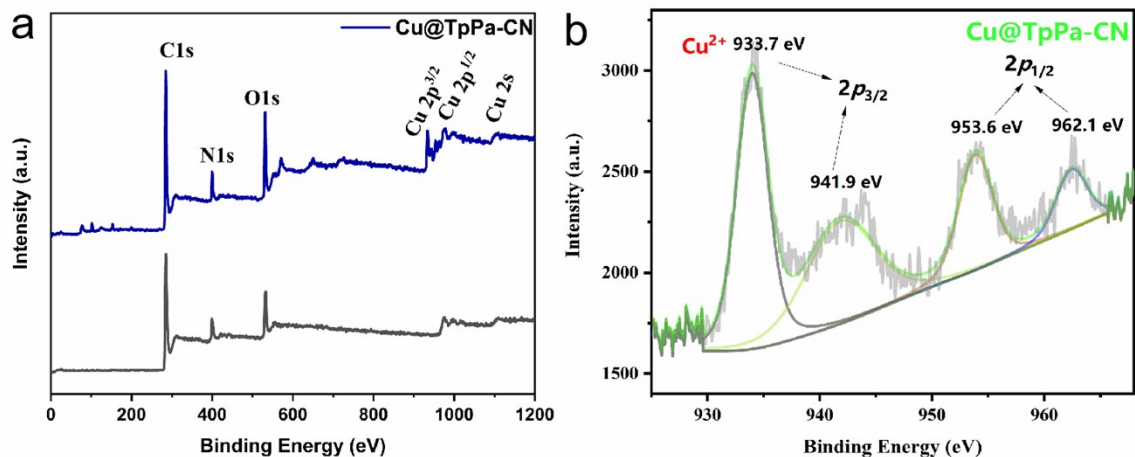
Figure S11. a) XPS full-spectrum image of TpPa-CN and Cu@TpPa-CN. b) High-resolution Cu 2p XPS spectra of Cu@TpPa-CN.

The XPS full-spectrum image suggested the presence of C, N, O, and Cu elements in Cu@TpPa-CN. The binding energy of 933.7 and 941.9 eV attributed to $2p_{3/2}$ of Cu^{2+} signals, and the peaks of 953.6 and 962.1 eV attributed to $2p_{1/2}$ of Cu^{2+} signals, respectively. For the same reason above, the Cu species exists as a single Cu^{2+} in Cu@TpPa-CN.
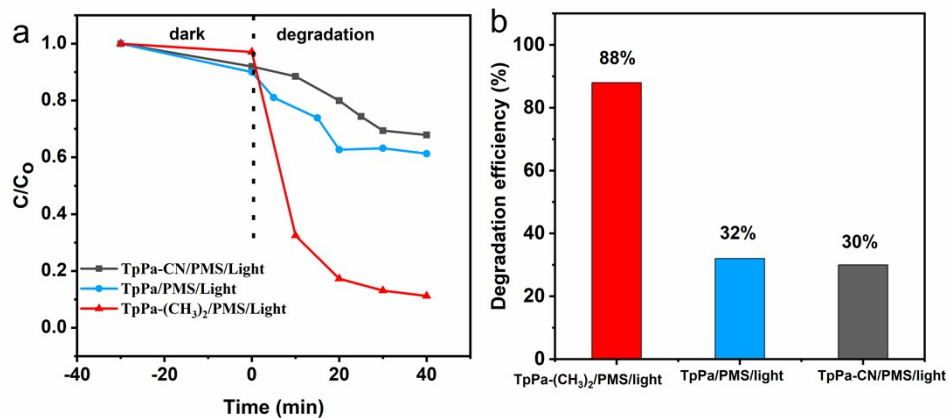
Figure S12 a) Photocatalytic activity of TpPa-X/PMS/Light (X=-(CH$_3$)$_2$, H, CN). b) The degradation efficiency for CBZ in TpPa-X/PMS/Light (X=-(CH$_3$)$_2$, H, CN).
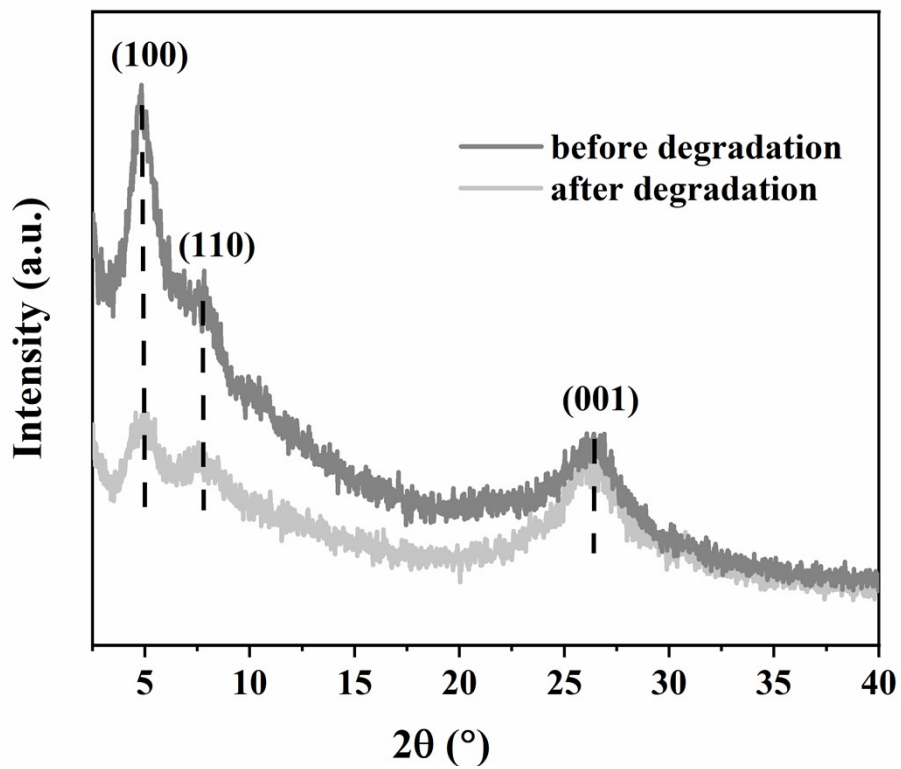
Figure S13. XRD patterns of Cu@TpPa-(CH$_3$)$_2$ before and after degradation of CBZ.
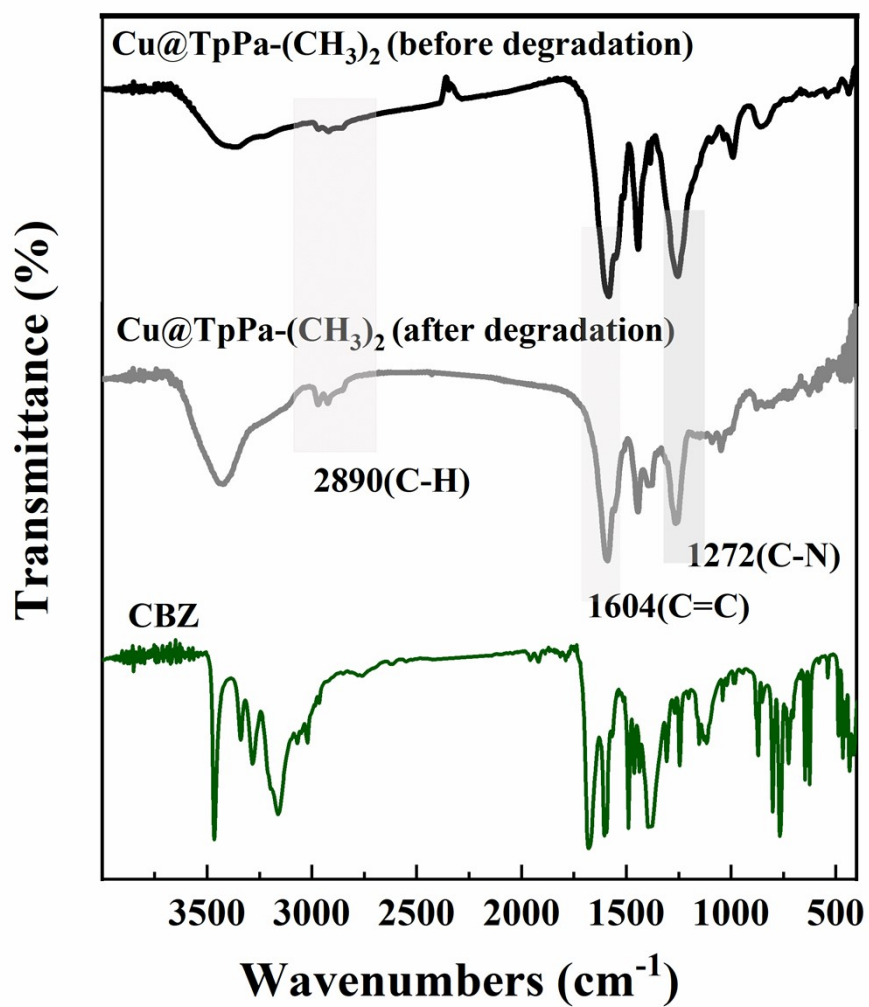
Figure S14. FITR spectrum of CBZ and Cu@TpPa-(CH$_3$)$_2$ before and after degradation.
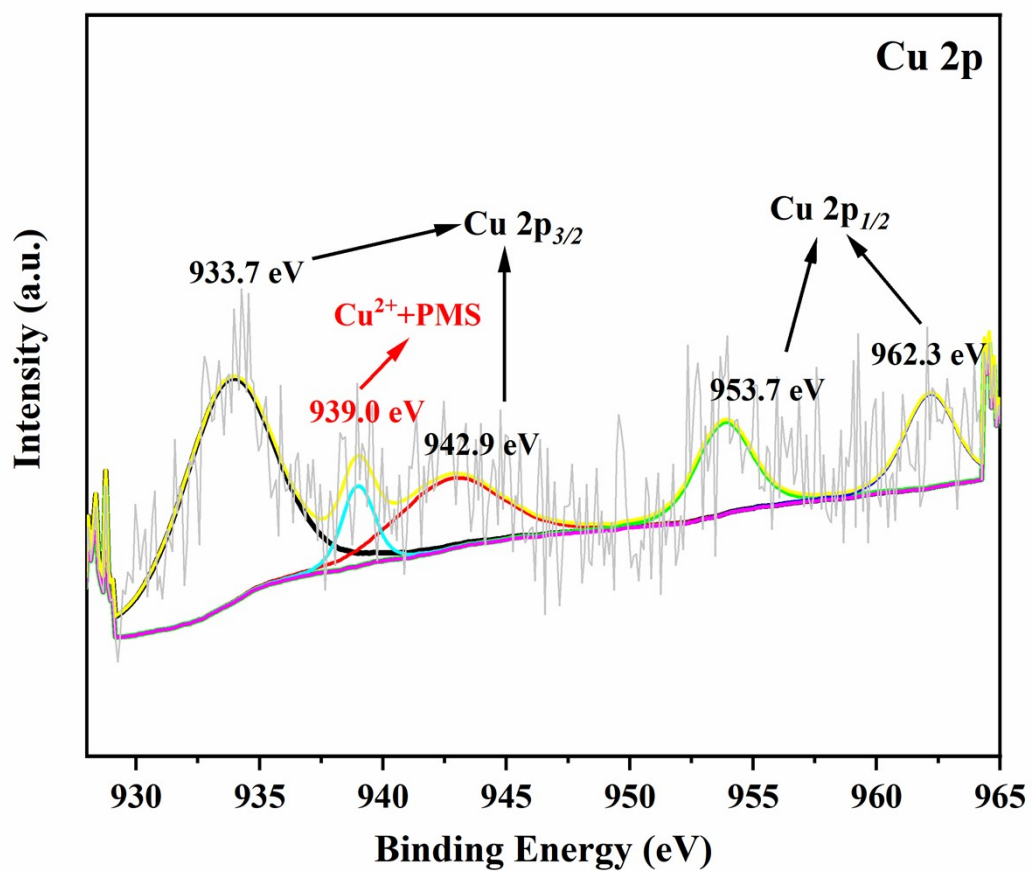
Figure S15. High-resolution Cu 2p XPS spectra of Cu@TpPa-(CH$_3$)$_2$ after degradation.
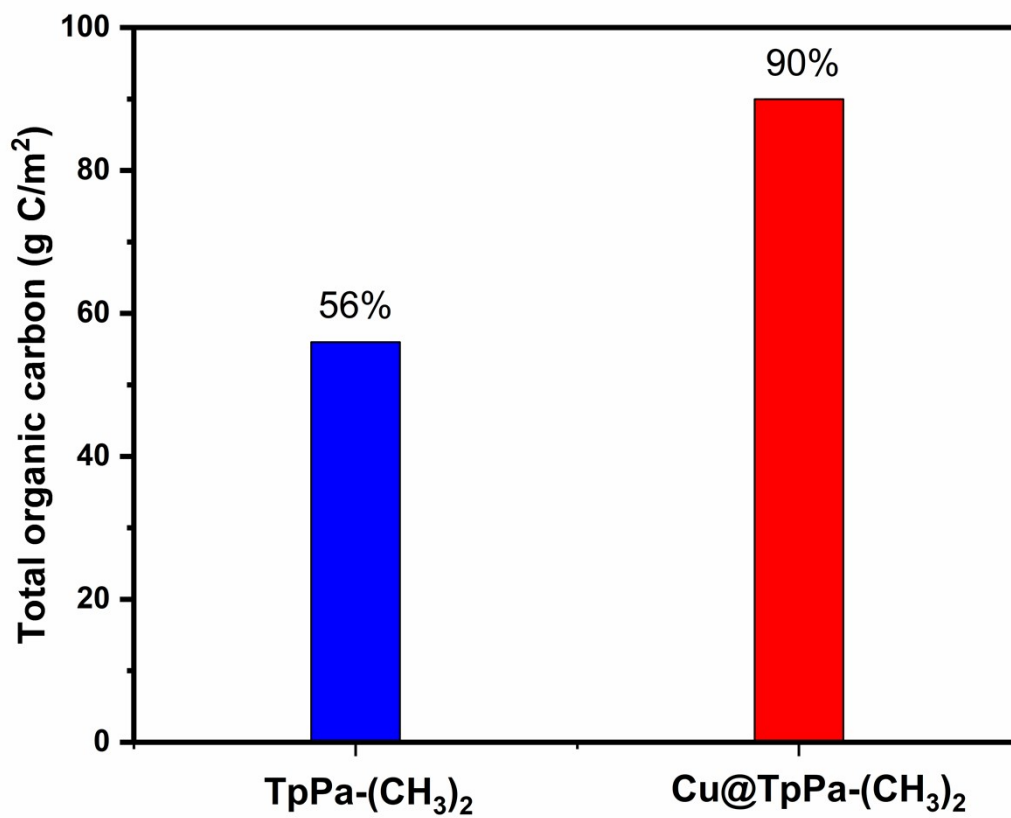
Figure S16. Total organic carbon content: degradation in Cu@TpPa-$(CH_3)_2$/PMS/Light and TpPa-$(CH_3)_2$/PMS/Light system, respectively.
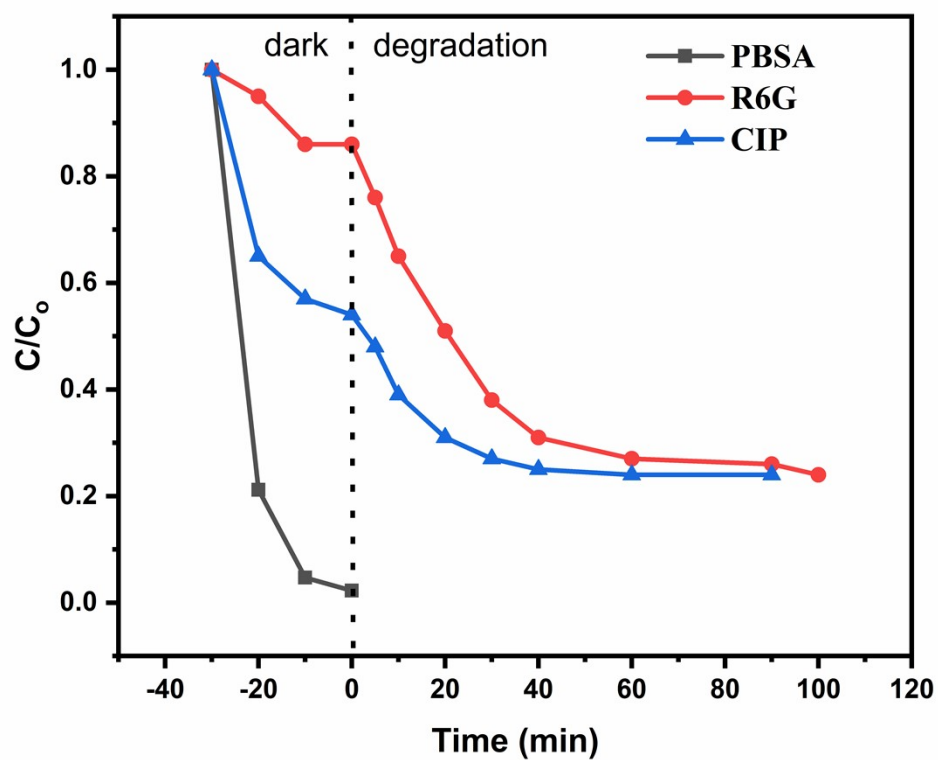
Figure S17. Photocatalytic activity of Cu@TpPa-(CH$_3$)$_2$/PMS/Light for PBSA, R6G and CIP degradation under light irradiation.
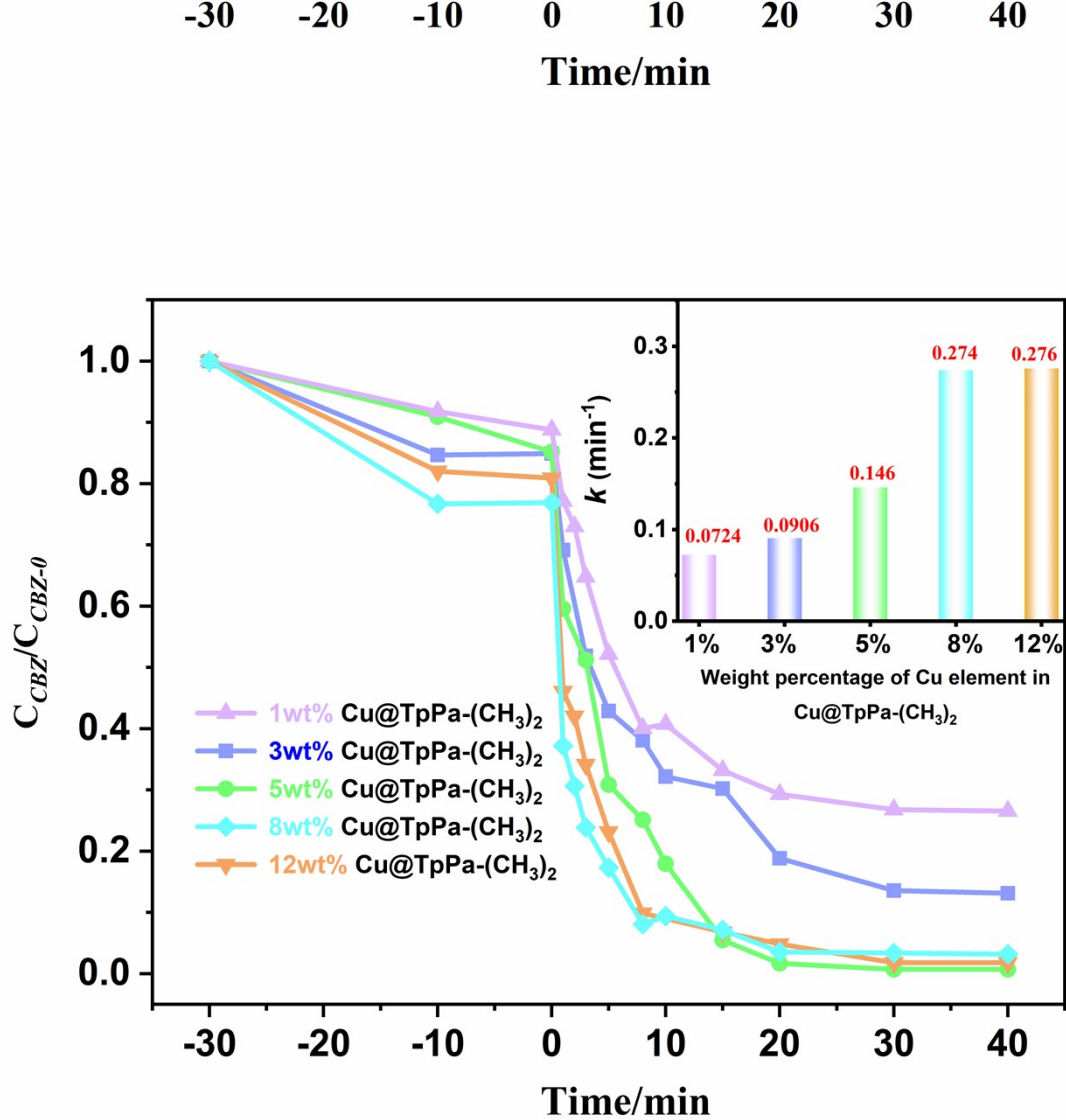
Figure S18. Influences of Cu^{2+} content on $TpPa-(CH_3)_2$ on the degradation of CBZ by Light/Cu@TpPa-$(CH_3)_2$/PMS system. Reaction condition parameters: [CBZ] = 10 mg/L, [catalyst] = 0.2 g/L, [PMS] = 1.0 mmol/L, initial pH = 7.0, and T = 25°C.
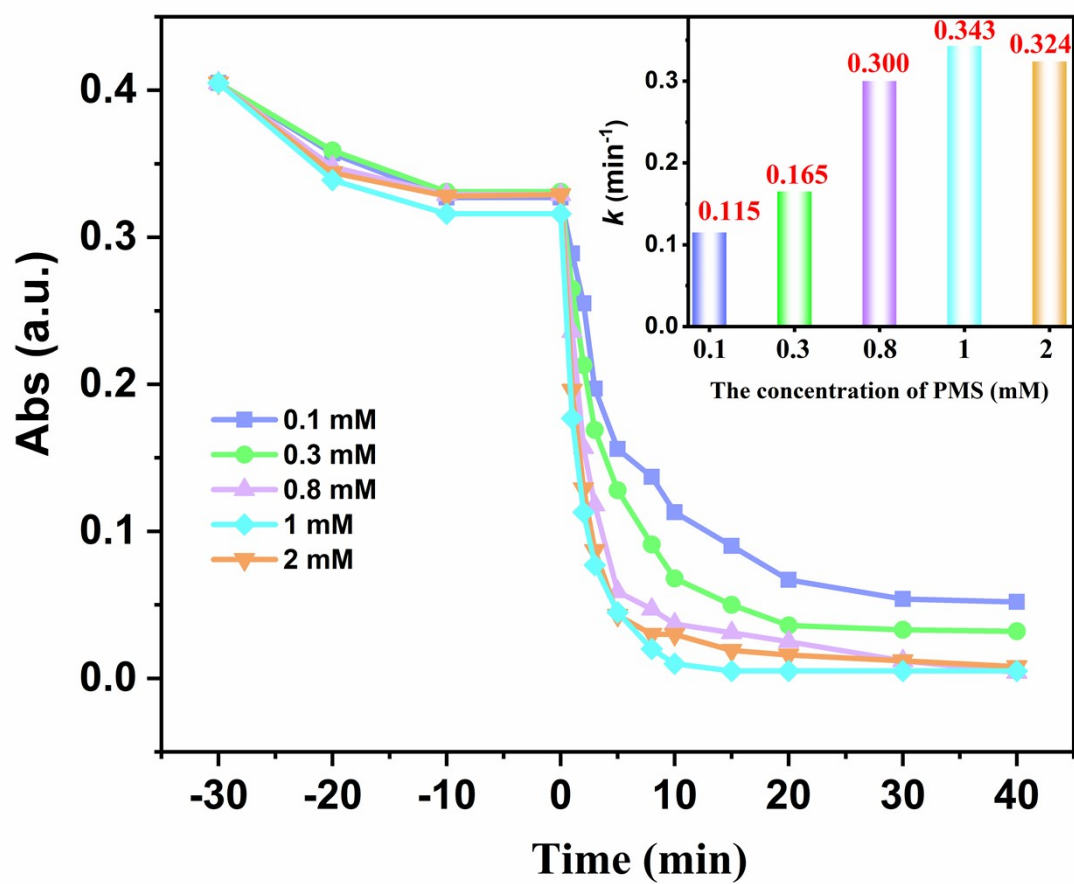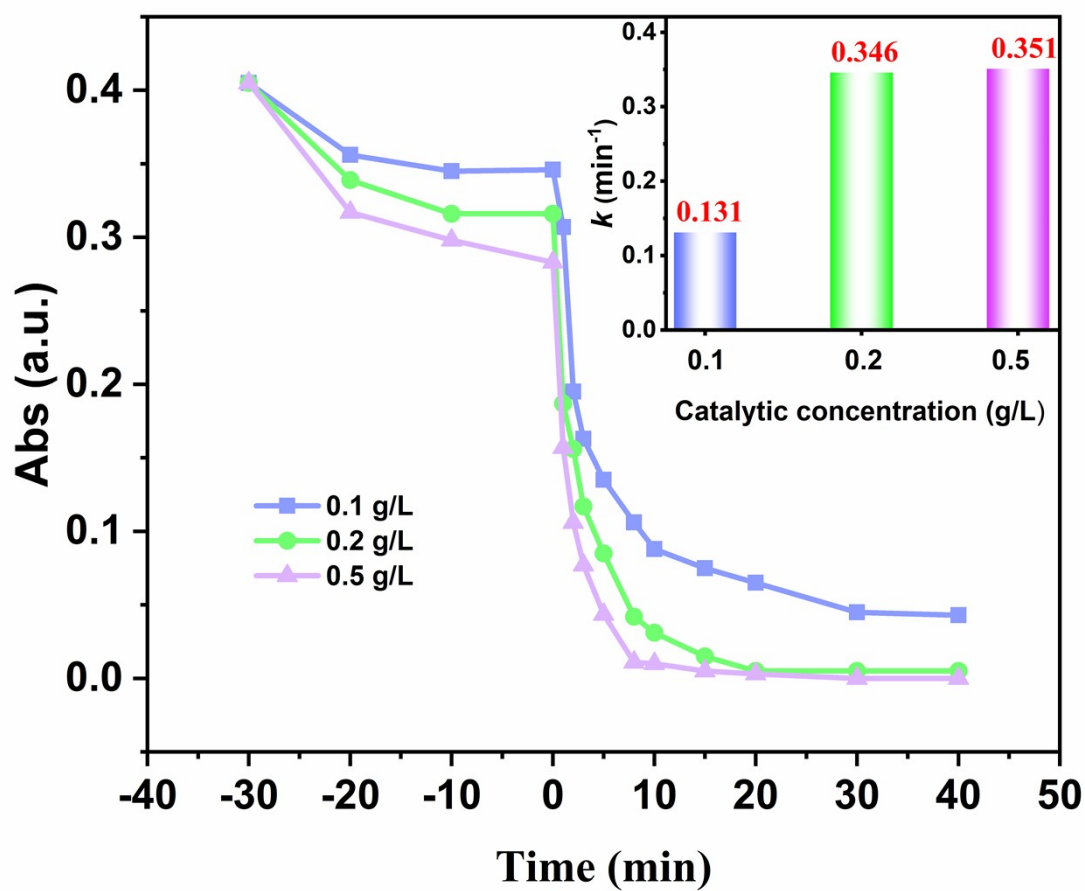
Figure S19. Influences of PMS concentration on the degradation of CBZ by Light/Cu@TpPa-(CH$_3$)$_2$/PMS system. Reaction condition parameters: [CBZ] = 10 mg/L, [catalyst] = 0.2 g/L, initial pH = 7.0, and T = 25°C.

Figure S20. Influences of catalytic concentration on the degradation of CBZ by Light/Cu@TpPa-(CH$_3$)$_2$/PMS system. Reaction condition parameters: [CBZ] = 10 mg/L, [PMS] = 1.0 mmol/L, initial pH = 7.0, and T = 25°C.
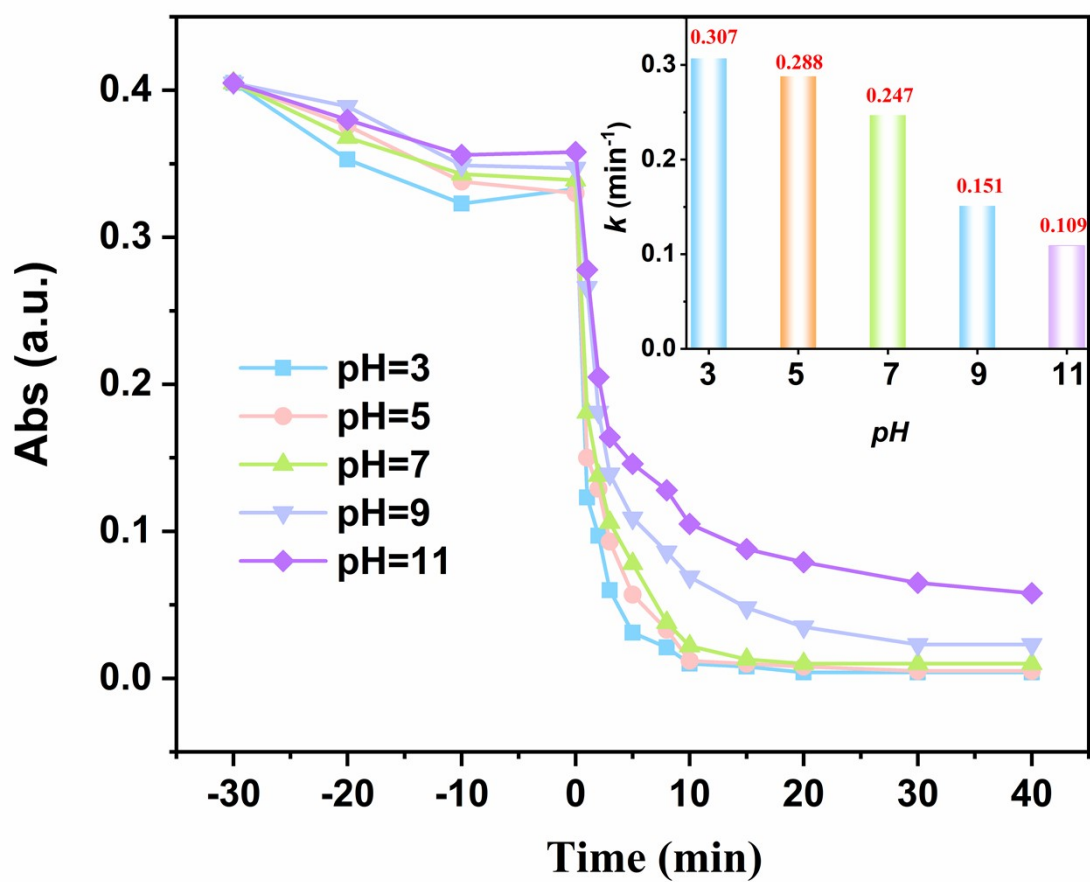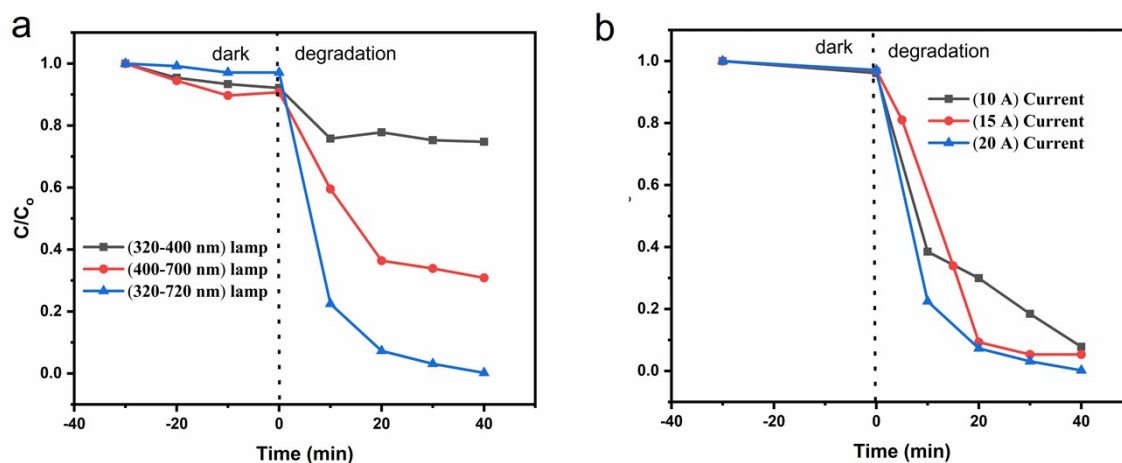
Figure S21. Influences of initial pH on the degradation of CBZ by Light/Cu@TpPa-(CH$_3$)$_2$/PMS system. Reaction condition parameters: [CBZ] = 10 mg/L, [catalyst] = 0.2 g/L, [PMS] = 1.0 mmol/L, and T = 25°C.

Figure S22: (a) Photocatalytic activity of Cu@TpPa-$(CH_3)_2$/PMS/Light for CBZ degradation under different wavelength ranges of light irradiation. (b) Photocatalytic activity of Cu@TpPa-$(CH_3)_2$/PMS/Light for CBZ degradation under different current light irradiation without optical filters and with the full wavelength range.
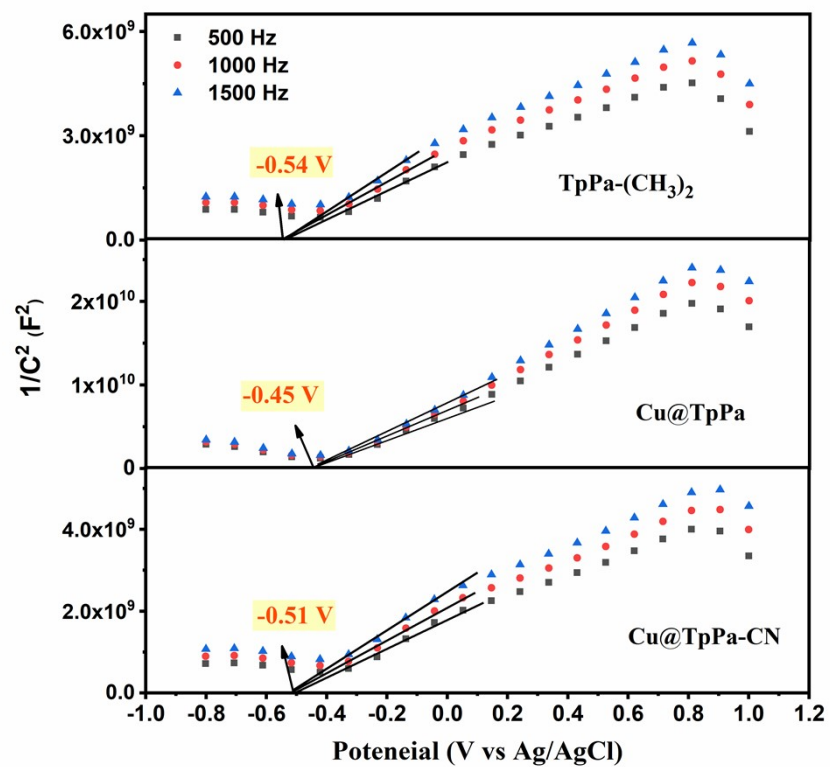
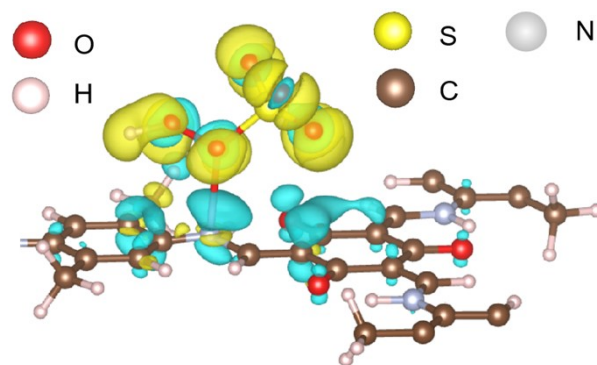**Figure S23.** Mott-Schottky curves of TpPa-$(CH_3)_2$, Cu@TpPa, and Cu@TpPa-CN.

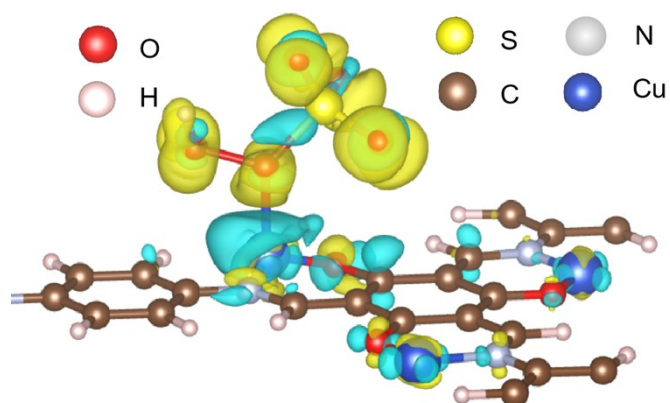**Figure S24.** Differential charge map (DCM) of TpPa-(CH$_3$)$_2$.

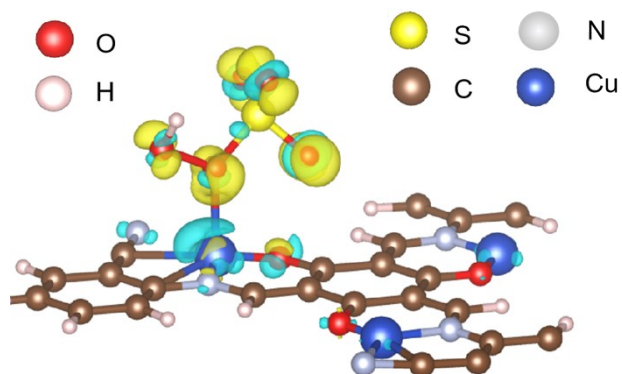**Figure S25.** Differential charge map (DCM) of Cu@TpPa.

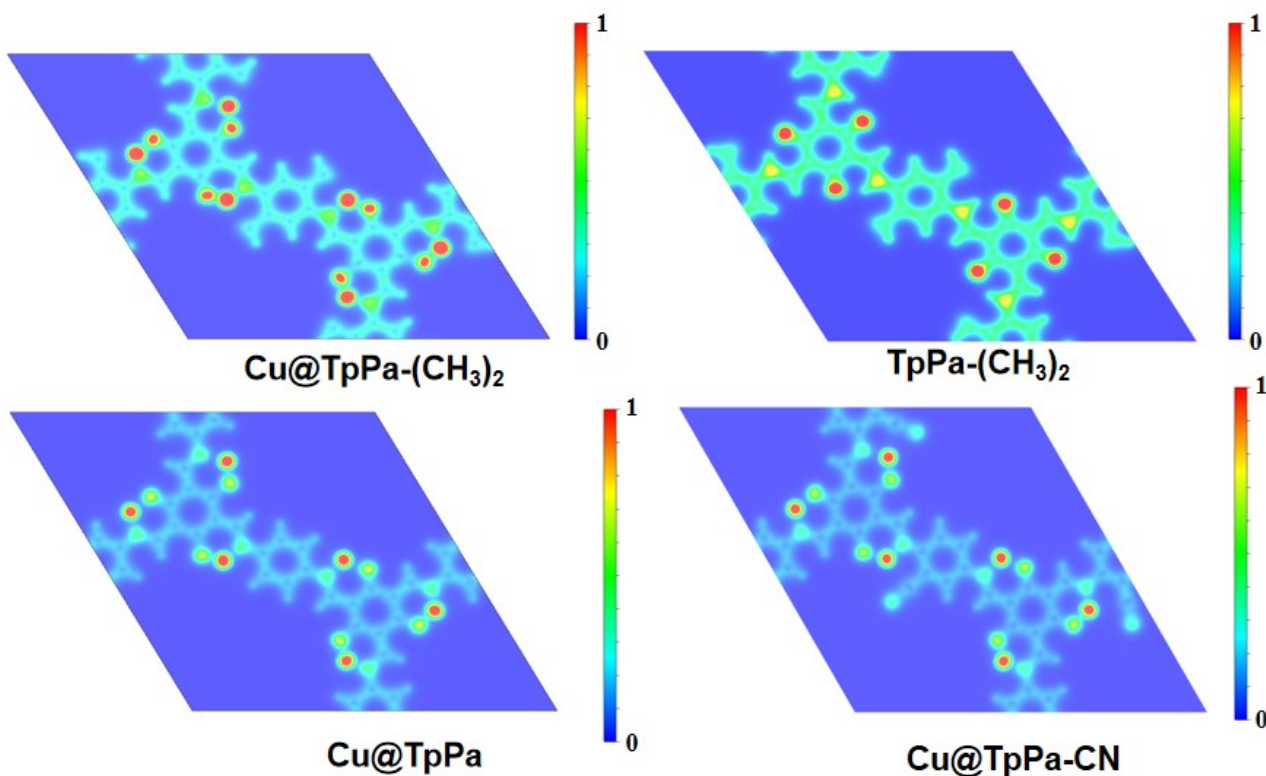**Figure S26.** Differential charge map (DCM) of Cu@TpPa-CN.

Figure S27. Equivalence diagram of electrostatic potential distribution of TpPa-$(CH_3)_2$ and Cu@TpPa-X, X=-($(CH_3)_2$, -H, and -CN).
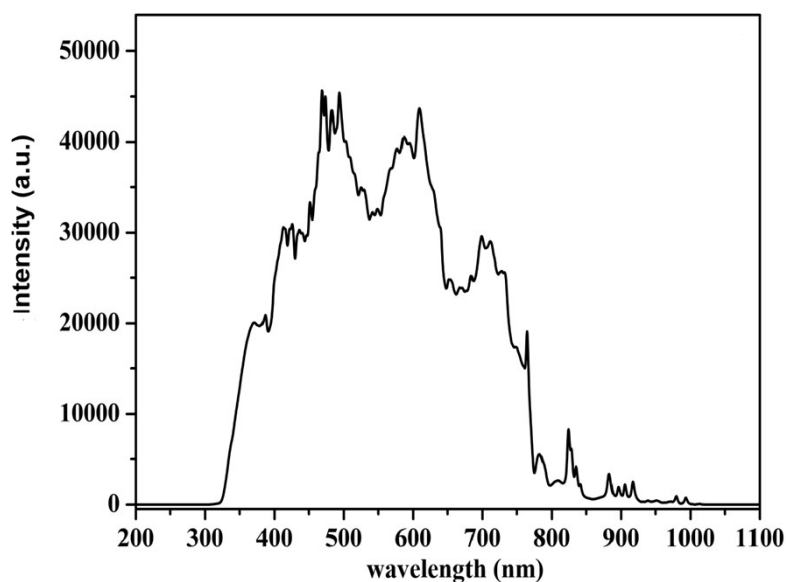

Figure S28. Emission spectrum of the PLS-SXE300Xenon lamp. (Courtesy of Perfect Light Co., Ltd., Beijing, China)
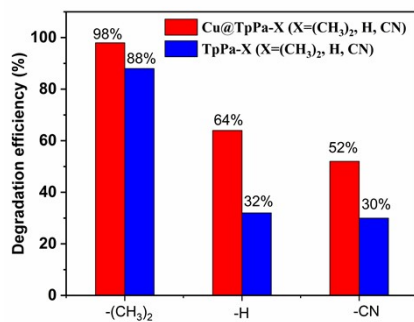
Figure S29. Fenton-like photodegradation efficiency of CBZ by different systems.

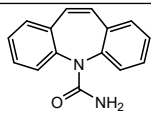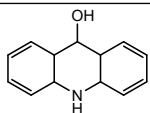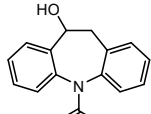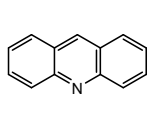**Table S1.** EXAFS data fitting results of Cu@TpPa-(CH$_3$)$_2$.
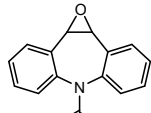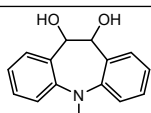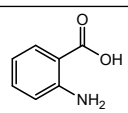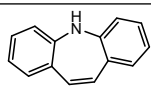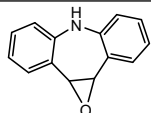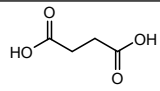
Sample	Path	CN^a	$R(Å)^b$	$\sigma^2 (Å^2)^c$	$\Delta E_0(eV)^d$	R factor
Cu K-edge (S_0^2=0.929)						
Cu foil	Cu-Cu	12*	2.540±0.002	0.0087	4.3	0.0023
Cu$_2$O	Cu-O	2.0±0.1	1.847±0.005	0.0026	7.5	0.0086
	Cu-O-Cu	12.1±0.3	3.026±0.013	0.0202	7.8	
	Cu-O	6.0±0.5	3.589±0.023	0.0156	7.5	
CuO	Cu-O	4.0±0.2	1.947±0.006	0.0043	6.2	0.0059
	Cu-O-Cu	4.0±0.3	2.868±0.018	0.0093	-4.6	
	Cu-O-Cu	6.1±0.6	3.373±0.022	0.0048		
Cu@TpPa-(CH$_3$)$_2$	Cu-N/O	2.2±0.2	1.955±0.014	0.0041	3.5	0.0066

[a]CN, coordination number; [b]R, the distance between absorber and backscatter atoms; [c]σ^2, the Debye Waller factor value; [d]ΔE_0, inner potential correction to account for the difference in the inner potential between the sample and the reference compound; R factor indicates the goodness of the fit. S_0^2 was fixed to 0.929, according to the experimental EXAFS fit of Cu foil by fixing CN as the known crystallographic value. * This value was fixed during EXAFS fitting, based on the known structure of Cu. Fitting conditions: k range：3.0 - 11.9; R range: 1.0-2.5; fitting space: R space; and k-weight = 3. A reasonable range of EXAFS fitting parameters: $0.800 < S_0^2 < 1.000$; $CN > 0$; $\sigma^2 > 0$ Å^2; $|\Delta E_0| < 15$ eV; and R factor < 0.02.

Table S2. Summary of PMS activation by heterogeneous catalysts to remove CBZ.

Catalysts	Conditions	CBZ (mg/L)	Degradation efficiency	k (min^{-1})	Mineralization rate	Ref.
HYSCN-8	PMS = 0.4 mM	5.0	> 96.0% (30 min)	0.108	/	2
CoP/N-g-C$_3$N$_4$	PMS = 0.6 mM	2.0	100.0% (30 min)	0.128	/	3
TS-Co$_3$O$_4$	PMS = 0.6 mM	5.0	100.0% (30 min)	0.079	/	4
C/BiOBr/CeO$_2$	Light: 500 W Xe lamp	20	86.0% (120 min)	0.0281	20%	5
BiOBr/g-C$_3$N$_4$	Light: 500 W Xe lamp	5	99% (300 min)	0.156	25%	6
Ag$_2$O/P-25	Light: 14 W Hg lamp	20	91.7% (180 min)	0.0152	67.9%	7
Si-doped TiO$_2$	PMS = 1 mM Light: 500 W Xe lamp	10	100% (60 min)	0.199	/	8
BiOCl	PMS = 1 mM Light: 500 W Xe lamp	10	99% (20 min)	0.108	20%	9
EHPDI/TiO$_2$	PMS = 0.2 mM Light: 300 W Xe lamp	5	98% (30 min)	0.131	75.2%	10
NV-gC$_3$N$_4$	PMS=0.5 mM Light: 500 W halogen tungsten lamp	10	97% (120 min)	0.0187	10%	11
B-gC$_3$N$_4$	PMS=0.5 mM Light: 35 W cold LED	10	90% (90 min)	0.0157	51%	12
Bis-PDI-T@TiO$_2$	PMS=1 mM Light: 300 W Xe lamp	10	98% (30min)	0.119	32%	13
Bi$_2$S$_3$/BiVO$_4$ /MgIn$_2$S$_4$	PMS = 0.5 mM, Light: 300 W Xe lamp	5.0	98.0% (30 min)	0.22	/	14
g-C$_3$N$_4$	PMS = 0.5 mM Light: 45 W LED	0.5	63.0% (90 min)	0.0211	/	15
Cu@TpPa-(CH$_3$)$_2$	**PMS = 1 mM Light: 50 W Xe lamp**	**10**	**98% (15 min)**	**0.322**	**90%**	**This work**

Table S3. List of transformation products generated by Light/PMS/Cu@TpPa-(CH$_3$)$_2$ process.

Compound	Elemental Composition	Proposed Structure	m/z	Compound	Elemental Composition	Proposed Structure	m/z
CBZ	C$_{15}$H$_{12}$N$_2$O		237	**P6**	C$_{13}$H$_9$N$_1$O$_1$		198
P1	C$_{15}$H$_{12}$N$_2$O$_2$		253	**P7**	C$_{13}$H$_9$N$_1$		180
P2	C$_{15}$H$_{12}$N$_2$O$_2$		253	**P8**	C$_6$H$_7$N		94
P3	C$_{15}$H$_{14}$N$_2$O$_3$		271	**P9**	C$_8$H$_7$NO$_4$		139
P4	C$_{15}$H$_{16}$N		210	**P10**	C$_6$H$_2$O$_2$		110
P5	C$_{14}$H$_{11}$N$_1$O		210	**P11**	C$_4$H$_6$O$_4$		119

.

References

1   J He, X. Jiang, F. Xu, C. Li, Z. Long, H. Chen and X. Hou, *Angew. Chem. Int. Ed,* 2021, **60**, 9984-9989.
2   Z. Wu, Z. Xiong, R. Liu, C. He, Y. Liu, Z. Pan, G. Yao and B. Lai, *J. Hazard Mater,* 2022, **427**, 128204.
3   C. Dong, Z. Zheng, Z. Wang, J. He, Z. Ye, X. Gong and I. M. C. Lo, *J. Hazard Mater,* 2021, **416**, 125891.
4   Q. Ma, Y. Zhang, X. Zhu and B. Chen, *J. Hazard Mater,* 2022, **427**, 127890.
5   L. Liang, S. Gao, J. Zhu, L. Wang, Y. Xiong, X. Xia and L. Yang, *Chem. Eng. J,* 2020, **391**, 123599.
6   L. Yang, L. Liang, L. Wang, J. Zhu, S. Gao and X. Xia, *Appl. Surf. Sci,* 2019, **473**, 527-539.
7   K. Gurung, M. C. Ncibi, S. K. Thangaraj, J. Jänis, M. Seyedsalehi and M. Sillanpää, *Sep. Purif. Technol*, 2019, **215,** 317-328.
8   Y. Zhou, H. Zhang, L. Wu, Y. Zhang, X. Wang and Z. Wu, *Chem. Eng. J,* 2023, **457**, 141234.
9   Y. Fang, H. Wang, X. Wang, Y. Zhou, L. Wu, W. D. Wu and Z. Wu, *Sep. Purif. Technol,* 2023, **307**, 122771.
10   L. Yang, Y. Jia, Y. Peng, P. Zhou, D. Yu, C. Zhao, J. He, C. Zhan and B. Lai, *Sci. Total Environ*, 2021, **783**, 146996.
11   J. Cao, W. Nie, L. Huang, Y. Ding, K. Lv and H. Tang, *Appl. Catal. B Environ*, 2019, **241**, 18-27.
12   M. Cui, K. Cui, X. Liu, X. Chen, Z. Guo, Y. Chen and C.-X. Li, *J. Hazard Mater,* 2021, **418**, 126338.
13   L. Yang, X. Hao, D. Yu, P. Zhou, Y. Peng, Y. Jia, C. Zhao, J. He, C. Zhan and B. Lai, *Sep. Purif. Technol,* 2021, **263**, 118384.
14   Y. Guo, Y. Ao, P. Wang and C. Wang, *Appl. Catal. B Environ*, 2019, **254**, 479-490.
15   Z. Cheng, L. Ling, J. Fang and C. Shang, *Chemosphere,* 2022, **286**, 131906.